

The evolution of merger fraction of galaxies at $z < 0.6$ depending on the star formation mode in the AKARI NEP–Wide field

Eunbin Kim^{1*†}, Ho Seong Hwang^{1,2,3}, Woong-Seob Jeong¹, Seong Jin Kim³, Denis Burgarella⁴, Tomotsugu Goto³, Tetsuya Hashimoto^{3,5}, Young-Soo Jo¹, Jong Chul Lee¹, Matthew Malkan¹², Chris Pearson^{18,19,20}, Hyunjin Shim⁶, Yoshiki Toba^{7,8,9}, Simon C.-C. Ho³, Daryl Joe Santos³, Hiroyuki Ikeda^{10,11}, Helen K. Kim¹², Takamitsu Miyaji^{13,14}, Hideo Matsuhara^{15,16}, Nagisa Oi¹⁷, Toshinobu Takagi²¹, Ting-Wen Wang³

¹Korea Astronomy and Space Science Institute, 776 Daedeokdae-ro, Yuseong-gu, Daejeon 34055, Korea

²Astronomy Program, Department of Physics and Astronomy, Seoul National University, 1 Gwanak-ro, Gwanak-gu, Seoul 08826, Korea

³SNU Astronomy Research Center, Seoul National University, 1 Gwanak-ro, Gwanak-gu, Seoul 08826, Republic of Korea

⁴Institute of Astronomy, National Tsing Hua University No. 101, Section 2, Kuang-Fu Road, Hsinchu 30013, Taiwan

⁵Aix Marseille Université, CNRS, Laboratoire d’Astrophysique de Marseille UMR 7326, 13388 Marseille, France

⁶Centre for Informatics and Computation in Astronomy (CICA), National Tsing Hua University, 101, Section 2. Kuang-Fu Road, Hsinchu, 30013, Taiwan

⁷Department of Earth Science Education, Kyungpook National University, 80 Daehakro, Bukgu, Daegu 41566, Korea

⁸Department of Astronomy, Kyoto University, Kitashirakawa-Oiwake-cho, Sakyo-ku, Kyoto 606-8502, Japan

⁹Academia Sinica Institute of Astronomy and Astrophysics, 11F of Astronomy-Mathematics Building, AS/NTU, No.1, Section 4, Roosevelt Road, Taipei 10617, Taiwan

¹⁰Research Center for Space and Cosmic Evolution, Ehime University, 2-5 Bunkyo-cho, Matsuyama, Ehime 790-8577, Japan

¹¹National Astronomical Observatory of Japan, 2-21-1 Osawa, Mitaka, Tokyo 181-8588, Japan

¹²National Institute of Technology, Wakayama College, Gobo, Wakayama 644-0023, Japan

¹³Department of Physics and Astronomy, UCLA, 475 Portola Plaza, Los Angeles, CA 90095-1547, USA

¹⁴Instituto de Astronomía sede. Ensenada, Universidad Nacional Autónoma de México (UNAM), Km 107, Carret. Tij.-Ens., Ensenada, 22060, BC, México

¹⁵Leibniz Institut für Astrophysik Potsdam, An der Sternwarte 16, 14482 Potsdam, Germany

¹⁶Department of Space and Astronautical Science, The Graduate University for Advanced Studies, SOKENDAI, 3-1-1, Yoshinodai, Chuo-ku, Sagamihara, Kanagawa 252-5210, Japan

¹⁷Institute of Space and Astronautical Science, Japan Aerospace Exploration Agency, 3-1-1 Yoshinodai, Chuo-ku, Sagamihara, Kanagawa, 252-5210, Japan

¹⁸Tokyo University of Science, 1-3, Kagurazaka Shinjuku-ku Tokyo 162-8601 Japan

¹⁹RAL Space, STFC Rutherford Appleton Laboratory, Didcot, Oxfordshire, OX11 0QX, UK

²⁰Oxford Astrophysics, University of Oxford, Keble Rd, Oxford OX1 3RH, UK

²¹The Open University, Milton Keynes, MK7 6AA, UK

²²Japan Space Forum, 3-2-1, Kandasurugadai, Chiyoda-ku, Tokyo 101-0062, Japan

Accepted XXX. Received YYY; in original form ZZZ

arXiv:2108.07125v1 [astro-ph.GA] 16 Aug 2021

ABSTRACT

We study the galaxy merger fraction and its dependence on star formation mode in the 5.4 square degrees of the North Ecliptic Pole-Wide field. We select 6352 galaxies with AKARI 9 μm detections, and identify mergers among them using the Gini coefficient and M_{20} derived from the Subaru/HSC optical images. We obtain the total infrared luminosity and star formation rate of galaxies using the spectral energy distribution templates based on one band, AKARI 9 μm . We classify galaxies into three different star formation modes (i.e. starbursts, main sequence, and quiescent galaxies) and calculate the merger fractions for each. We find that the merger fractions of galaxies increase with redshift at $z < 0.6$. The merger fractions of starbursts are higher than those of main sequence and quiescent galaxies in all redshift bins. We also examine the merger fractions of far-infrared detected galaxies which have at least one detection from *Herschel*/SPIRE. We find that *Herschel* detected galaxies have higher merger fraction compared to non-*Herschel* detected galaxies, and both *Herschel* detected and non-*Herschel* detected galaxies show clearly different merger fractions depending on the star formation modes.

Key words: galaxies: evolution – galaxies: formation – galaxies: spiral – galaxies: starburst – galaxies: star formation – infrared : galaxies

1 INTRODUCTION

Galaxy interactions and mergers are thought to play an important role in galaxy evolution, impacting their morphologies, gas kinematics, and star formation rates (Toomre & Toomre 1972; Sanders et al. 1988; Barnes & Hernquist 1996; Conselice 2006). Cold dark matter models predict that galaxies have accreted their mass through hierarchical mergers (De Lucia et al. 2006). Mergers are also suspected to trigger luminosity increases, from active galactic nuclei (AGNs, Sanders & Mirabel 1996) and starbursts (Barnes & Hernquist 1996; Mihos & Hernquist 1996; Cox et al. 2006). Enhanced star formation can result from the tidal interactions of the galaxies that compress/shock the gas, causing it to collapse and form stars (Barnes 2004; Kim, Wise & Abel 2009; Saitoh et al. 2009). These merger-induced starbursts are sometimes observed as luminous/ultra-luminous infrared galaxies (LIRGs/ ULIRGs), which have extreme far-infrared (FIR) luminosities of $10^{11} L_{\odot}$ and $10^{12} L_{\odot}$, respectively (Sanders & Mirabel 1996). Several studies have shown that the infrared luminosity of galaxies is statistically correlated with mergers (Ellison et al. 2013; Larson et al. 2016). These can be seen as morphological disturbances in LIRGs and ULIRGs (Elbaz & Cesarsky 2003; Hwang et al. 2007; Hwang & Park 2009; Kartaltepe et al. 2010; Ellison et al. 2013).

However, the merger contributions to starbursts in general is still unclear. At high redshifts, average star formation rates are higher. LIRGs and ULIRGs are often found on the “main sequence”, that is, obeying the correlation between SFR and stellar mass of typical galaxies at a given redshift (Daddi et al. 2007; Elbaz et al. 2007). Thus, we will define starbursts by comparison with the star formation of other galaxies of a given stellar mass in the same redshift bin. Previous studies have defined starbursts as galaxies experiencing star formation three or four times above the median of the SFRs of main sequence of star-forming galaxies (El-

baz et al. 2011; Rodighiero et al. 2011; Schreiber et al. 2015). In a similar way, we divide galaxies into three different star formation “modes” (i.e. starbursts, main sequence and quiescent galaxies) in each redshift bin.

It is challenging to identify a large number of merger galaxies out to large redshifts. There are two main methods to identify mergers – selecting close pairs (Bundy et al. 2009; de Ravel et al. 2009; Man, Zirm & Toft 2016; Duncan et al. 2019) or using morphological disturbances (Conselice et al. 2003; Lotz et al. 2008, 2011). For example, Kado-Fong et al. (2018) used the Subaru/HSC images to select the merger galaxies at $0.05 < z < 0.45$ using visually identified tidal features (e.g. shell or stream features) However, for using close pairs, spectroscopic velocities for both pairs are needed. Because spectroscopic observations are expensive, merger studies based on them will suffer from incompleteness. Deep and high-resolution imaging (e.g. *Hubble Space Telescope*) could avoid that incompleteness, but the merger fraction from galaxy imaging may be ambiguous. Morphological disturbances presented the late-stage of mergers can be determined by visual inspection or discriminate quantitative outliers of morphological disturbances. Visual inspection is subjective and time-consuming. High redshift galaxies can also be easily misclassified because of wavelength-dependent morphology and surface brightness effects (Bolin et al. 1991; Kuchinski et al. 2000; Windhorst et al. 2002; Kampczyk et al. 2007).

In general, morphological types of galaxies are classified by the light profiles of galaxies. The measured profile is the average intensity of a galaxy as a function of radius, and can be mathematically fitted (e.g. Sérsic profile, Sersic 1963). These parametrizations historically have been used to classify galaxies into Ellipticals, Spirals and Irregular galaxies. There are also non-parametric measures for galaxy classification, such as concentration, asymmetry, clumpiness (CAS, Conselice, Bershadsky & Jangren 2000; Conselice et al. 2003; Menanteau et al. 2006). In addition, there have been many studies of morphological classification using the parameters of Gini coefficient and M_{20} (Lotz, Primack & Madau 2004; Lotz et al. 2008). The Gini coefficient is a mea-

* Contact e-mail:ebkim@si-analytics.ai

† Present Address: SI-analytics, Yuseungdaero 1689 gil 70, Yuseung-gu, Daejeon, 34047, Korea

sure whether the flux of a galaxy is concentrated or spread out (to be formally defined in Section 3), and M_{20} is the second-order moment of the brightest 20 percent of a galaxy (Lotz, Primack & Madau 2004; Lotz et al. 2008). The Gini coefficient is originally used in economics to statistically describe the distribution of wealth within a society. This coefficient was applied to astronomical images to quantify the spread of galaxy light (Abraham et al. 2003; Lotz et al. 2008), which is now widely used for morphological analysis in astronomy. Between these two approaches (parametric vs. non-parametric), non-parametric measurements may be less impacted by redshift. Concentration, asymmetry, clumpiness are used for merger-finding, but asymmetry measurement is less sensitive to the late-stage of mergers (Lotz et al. 2008). The Gini coefficient and M_{20} are used for wide area surveys (Lotz, Primack & Madau 2004; Lotz et al. 2010a,b). These parameters are more effective in classifying galaxies and identifying late-stage mergers than concentration and asymmetry, and also more robust for galaxies with low signal-to-noise ratios (Lotz, Primack & Madau 2004; Lotz et al. 2008). Therefore, we use the Gini coefficient and M_{20} for identifying mergers, for quantitative comparison with other studies, and to secure a large sample from our data.

In this paper, we examine the evolution of merger fractions of galaxies with redshifts up to $z = 0.6$ in the AKARI North Ecliptic Pole (NEP)–Wide field, and the variations in merger fractions of galaxies in three different star-formation modes (i.e. starbursts, main sequence, and quiescent galaxies). We also study how the FIR detection affects the merger fractions. In Section 2, we summarise our observational data and sample selection. Section 3 describes the morphological analysis to classify the galaxies using the Gini and M_{20} . We present the results and discussion in Sections 4 and 5, respectively.

2 DATA

2.1 Optical images

We use deep optical images taken with the Hyper Supreme-Cam (HSC) on Subaru 8-m telescope in the AKARI NEP–Wide field covering 5.4 deg^2 (Goto et al. 2017, Oi et al. in accepted). The HSC has a 1.5 deg field of view (FoV) covered with 104 red-sensitive CCDs, and the pixel scale is 0.17 arcsec . It is the largest FoV among the 8-m telescopes, and the size of FoV covered the AKARI NEP–Wide field with only four pointings (see Figure 2 in Goto et al. 2017, Figure 1 in Oi et al. in accepted). The observations of the NEP–Wide field were performed in June 30th 2014 and August 7–10th in 2015. The 5σ detection limits are 28.6, 27.3, 26.7, 26.0, 25.6 AB mag, and the median seeings are 0.68, 1.26, 0.84, 0.76, 0.74 for g , r , i , z and y -band, respectively. The total number of identified sources in 5 bands is 3.5 million and more detailed information on the data set is described in Oi et al. (accepted).

2.2 Multi-wavelength Data

We have used the multi-wavelength data set based on the catalogue of AKARI mid-IR (MIR) galaxies newly identified

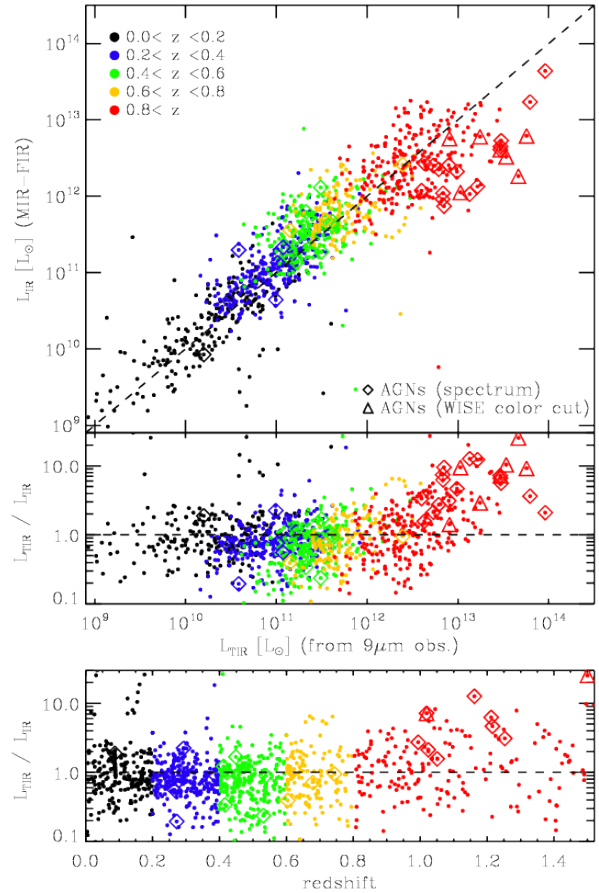


Figure 1. $L_{IR}(\text{MIR-FIR})$ versus L_{TIR} from AKARI $9 \mu\text{m}$ (Top). $L_{IR}(\text{MIR-FIR})$ is fitted by CIGALE including at least one FIR band detection (Wang et al. 2020). Diamonds and triangles represent AGNs classified with spectra and WISE colour cut, respectively. (Middle) The ratio of the L_{TIR} to $L_{IR}(\text{MIR-FIR})$ as a function of L_{TIR} . (Bottom) The ratio of the L_{TIR} to $L_{IR}(\text{MIR-FIR})$ as a function of redshift. Colour codes represent galaxies in different redshift ranges.

by an optical survey by Subaru/HSC (Oi et al. 2021). The infrared galaxies detected by AKARI’s NEP–Wide survey (Kim et al. 2012) were cross-matched against deep HSC optical data, thereafter all available supplementary data over the NEP–Wide field were merged together (Kim et al. 2021).

Data merging of these two catalogues were carried out by positional matching with the matching radii defined by 3-sigma positional offsets, which are more rigorous than using PSF sizes (Kim et al. 2021). This band-merged catalogue has 91,000 objects including $\sim 70,000$ objects detected in N2, N3, N4 bands, $\sim 20,000$ objects detected in S7, S9, L11, L18, L24 bands, and is the reference catalogue for our sample selection in this study. Optical to submillimeter (submm) photometry for AKARI sources are also added. Original AKARI NEP–Wide field catalogue (Kim et al. 2012) includes CFHT/MegaCam u^* , g' , r' , i' , z' (Hwang et al. 2007), Maidanak observatory/SNUCAM B, R, I-band data (Jeon et al. 2010) and KPNO /FLAMINGOS J and H band data (Jeon et al. 2014). Supplementally, the observed data from CFHT/MegaPrime u -band (Huang et al. 2020),

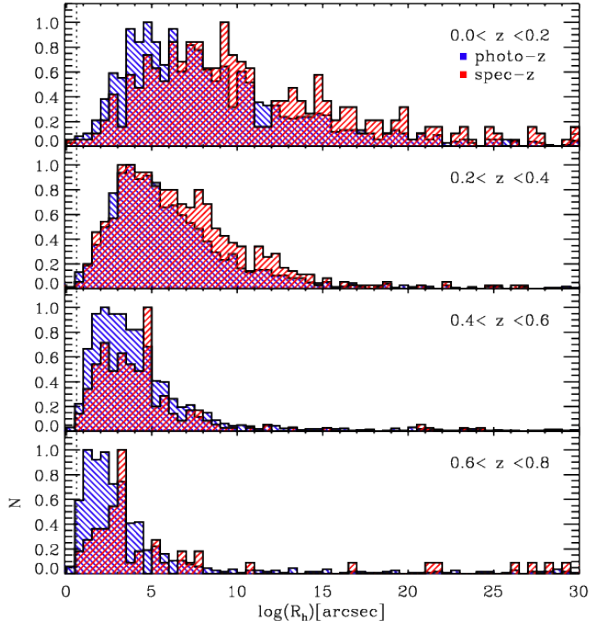


Figure 2. Distribution of radius for galaxies. Dotted line represents the seeing size, 0.6 arcsec in the HSC *i*-band image. Blue and red histograms represent the galaxies with photo-*z* and spec-*z*.

CFHT/MegaCam u^* , g' , r' , i' , z' (Oi et al. 2014; Goto et al. 2018), WIRCam Y, J and Ks band (Oi et al. 2014) are added to the main catalogue. The main catalogue is also cross-matched with the *WISE* catalogue (Jarrett et al. 2011), *Spitzer*/IRAC (Nayyeri et al. 2018) and *Herschel*/PACS and SPIRE (Pearson et al. 2017, 2019). This band-merged catalogue adopted spectroscopic redshifts for objects from several observations, which include Keck/DEIMOS (Shogak et al. 2018; Kim et al. 2018) and MMT/Hectospec and WIYN/Hydra (Shim et al. 2013). Subaru/FMOS (Oi et al. 2017), GTC (Miyaji et al. in preparation) and the SPICY survey (Ohyama et al. 2018) are also included. Photometric redshifts are determined (Ho et al. 2021) using 26 bands from optical to NIR with the public code LePhare (Arnouts et al. 1999; Ilbert et al. 2006), and the photo-*z* accuracy is $\sigma = 0.053$.

2.3 Physical Parameters of Galaxies

We derive the total infrared luminosity (L_{TIR} , 8–1000 μm) using a set of template spectral energy distributions (SEDs) of main sequence galaxies in Elbaz et al. (2011) with each of AKARI bands, S7, S9, S11, L15, L18 and L24. They defined a typical IR SED for main sequence galaxies using *Herschel* data, this SED could extrapolate the total IR luminosity for galaxies that only one measurement exists. Although L_{TIR} derived with FIR data could be more accurate than that without FIR data, the latter case enables us to secure a large number of samples (Calzetti et al. 2010; Galametz et al. 2013).

To assure the validity of the L_{TIR} from one-band, we compare the L_{TIR} with infrared luminosity (L_{IR} derived from MIR–FIR bands, Wang et al. 2020). They calculated the L_{IR} using SED modeling code CIGALE (Burgarella et

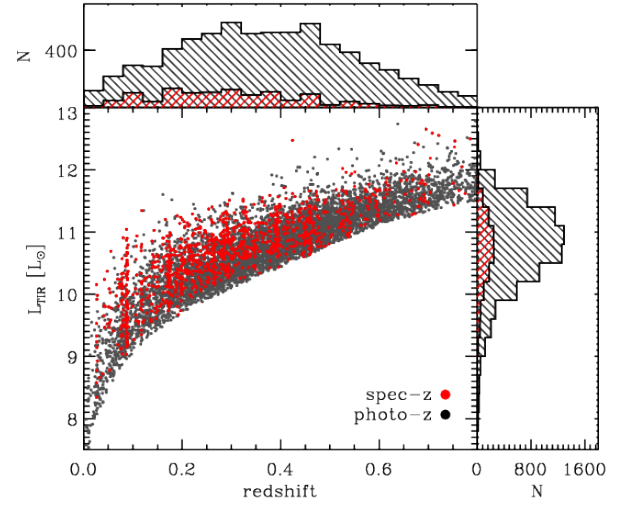


Figure 3. Total infrared luminosity distribution as a function of redshift for 9- μm selected galaxies. Black circles and red crosses represent the galaxies with spec-*z* and photo-*z*.

al. 2005; Noll et al. 2009) with 36 bands ranging from optical to submm bands, which is represented as a sum of dust and AGN activities.

As seen in Figure 1, we compared the difference between L_{TIR} from one-band and L_{IR} from MIR–FIR bands as a functions of L_{TIR} and redshift. L_{TIR} and L_{IR} up to around $L_{\text{TIR}} = 10^{13} L_{\odot}$ show good agreement below $z \sim 0.8$, which may originate from the effect of galaxy evolution on the SED over the cosmic time. The relation between the total IR luminosity and one-band IR luminosity could have discrepancy as redshift increases depending on which IR-band is used (e.g. 24 vs 8 μm , Elbaz et al. 2011). Since such a trend is commonly found in every AKARI MIR band (7–24 μm), we used 9 μm band (S9) for sample selection because of the largest number of sample. In the middle panel, the standard deviation in $L_{\text{IR}}/L_{\text{TIR}}$ of galaxies except AGNs is 0.71. A detailed sample selection is described in Section 2.4 and Table 1.

Since the L_{TIR} is usually used as good star formation indicator, we calculate the L_{TIR} from the initial mass function (IMF). We adopt the Salpeter (1955) initial mass function (IMF), which is also used for calculating L_{IR} with CIGALE in Wang et al. (2020). The star formation rates are calculated from the formula (12) in Kennicutt & Evans (2012) which is

$$\log \dot{M}_* (\text{M}_{\odot} \text{year}^{-1}) = \log L_x - \log C_x, \quad (1)$$

where L_x units are [ergs s^{-1}] and $\log C_x = 43.41$ adopting the calibration factors from Hao et al. (2011); Murphy (2011). The stellar mass (M_*) is derived from SED fitting with LePhare (Arnouts et al. 1999; Ilbert et al. 2006) using 13 multi-wavelength data of CFHT/MegaCam u' , Subaru/HSC g , r , i , z , Y, CFHT/Wircam J, Ks, and AKARI N2, N3, N4, S7, S9 bands. We convert M_* from LePhare based on Chabrier (2003) IMF to M_* based on Salpeter (1955) IMF by dividing by a factor of 0.63 to fairly compare with others (e.g. Schreiber et al. 2015; Pearson et al. 2018).

The star forming galaxies in the main sequence follow an empirical power-law relation between the SFR and stellar

Table 1. Number of Galaxies with 5-sigma detection in different AKARI/IRC bands

Band	S7	S9	S11	L15	L18	L24
Total	5007	9076	9099	8592	10133	2384
spec-z	1022	1417	1388	1117	1186	532
photo-z	5003	9072	9096	8589	10130	2382
<hr/>						
Total ($z < 0.8$)	3702	7236	7377	4640	5068	1349
spec-z	861	1239	1220	927	971	443
photo-z	3659	7173	7317	4580	5010	1320
<hr/>						
Total ($z < 0.6$)	3407	6425	6200	3392	3805	1150
spec-z	820	1169	1137	849	893	413
photo-z	3348	6331	6107	3307	3718	1108
Herschel detection	739	1048	1051	805	853	467

mass. However, [Smercina et al. \(2018\)](#); [Draine et al. \(2020\)](#) showed that quiescent galaxies have considerable scatter on this relation when they compared different indicators such as L_{TIR} , $H\alpha$, neon lines, etc. Thus, considering to adopt separate conversion factor for deriving the SFR for each different star formation mode might improve the relation. However, because we have constrained galaxies with the range of $9.0 < \log(M_*/M_\odot) < 11.5$ including relatively massive quiescent galaxies, we do not apply the separate conversion factor for quiescent galaxies in this paper.

The star forming galaxies show tight correlations between L_{TIR} and SFR (e.g., [Kennicutt & Evans 2012](#); [Hwang et al. 2010, 2012](#)). However, this tight correlation can break down for quiescent galaxies, especially for those with low infrared luminosities (e.g., [Smercina et al. 2018](#); [Draine et al. 2020](#)). Thus, it is conceivable that this difference might affect our results. However, the infrared luminosities of our sample galaxies (even for quiescent galaxies) are generally high enough, the impact of this different correlation is insignificant.

2.4 Sample Selection

Considering the total number of detected sources at each AKARI band in the band-merged catalogue, we selected the S9 (9 μm) band for our study (see Table 1). The total number of galaxies in Table 1 presents the number of galaxies with redshift information estimated from either spectroscopic or photometric measurement. Although the total number of galaxies with L18 is the largest in the whole redshift range, we select 9 μm detected galaxies for our sample, because the number of galaxies is the largest at the redshift below $z = 0.6$ where we finally analyse the data. Note that the total number of 9 μm detected galaxies is 9,076 and it is reduced to be 7,236 and 6,425 at $z < 0.8$ and $z < 0.6$, respectively. To examine the contribution from AGNs in our analysis, we overplot 190 AGNs in Figure 1, which were identified by Baldwin-Phillips-Terlevich (BPT) emission-line ratio diagrams ([Shim et al. 2013](#)). In addition, 30 IR-bright AGNs are found through WISE W1 - W2 and W2 - W3 colour-colour diagrams with the criteria of [Jarrett et al. \(2011\)](#) and [Mateos et al. \(2012\)](#). Figure 1 shows that AGNs are significantly off the linear correlation of L_{TIR} and L_{IR} . This is because AGN-dominant galaxies have higher MIR luminosities compared to star-forming galaxies ([Spinoglio et al.](#)

[1995](#)). Due to these templates are based on star-forming galaxies, we remove these 219 AGNs (73 AGNs in $z < 0.6$) from the further analysis, and end up having 6,352 galaxies at $z < 0.6$.

Figure 2 shows the normalised histogram of distributions of seeing corrected half light radius (R_h) for galaxies in each redshift bin, from top to the bottom. We separate the redshift into the range of 0.2 bin and find most of galaxies in size are larger than the seeing 0.6 arcsec in the HSC i -band in all redshift bins. Figure 3 shows the distribution of sample galaxies on the redshift and the total infrared luminosity. Red and black circles represent the sample with spectroscopic and photometric redshifts, respectively. Upper and right panels show histograms of redshift and L_{TIR} , respectively.

3 MEASUREMENT OF MORPHOLOGICAL PARAMETERS

The morphological parameters allow us to classify the galaxy types. In order to quantify galaxy morphologies, we used the Gini coefficient and M_{20} classification method ([Lotz, Primack & Madau 2004](#)).

The Gini coefficient is a statistical measure of distribution of income in a population in economics, and recently has applied to astronomy as well ([Abraham et al. 2003](#); [Lotz, Primack & Madau 2004](#)). The Gini can be computed sorting the f_i pixel value increasing order as

$$G = \frac{1}{|\bar{f}|n(n-1)} \sum_{i=1}^n (2i - n - 1) |f_i| \quad (2)$$

where \bar{f} is the mean over the pixel values and n is the number of pixels. If all the flux of a galaxy is concentrated in one pixel, $G = 1$, while a galaxy has a homogeneous surface brightness, $G = 0$ ([Glasser 1962](#)).

The M_{20} is the second order moment of brightest regions of a galaxy. The brightest 20 % of the light is normalised to the total second-order central moment, M_{tot} ([Lotz, Primack & Madau 2004](#)). These are defined as

$$M_{tot} = \sum_i^n M_i = \sum_i^n f_i [(x_i - x_c)^2 + (y_i - y_c)^2], \quad (3)$$

$$M_{20} = \log_{10} \frac{\sum_i M_i}{M_{tot}}, \text{ while } \sum_i f_i < 0.2f_{tot}, \quad (4)$$

where f_i is the pixel flux value and x_c, y_c is the galaxy centre. The centre is the point where M_{tot} is minimised. The M_{20} is anti-correlated with concentration; low M_{20} represents highly concentrated galaxy.

We derive the non-parametric Gini and M_{20} using `statmorph` python code ([Rodriguez-Gomez et al. 2019](#)) on galaxies in cutouts of r and i -band images. It constructs a segmentation map for Gini measurements to be insensitive to dimming surface brightness for distant galaxies ([Lotz, Primack & Madau 2004](#)). The image of a galaxy is convolved with the Gaussian kernel $\sigma = r_{petro}/5$, where r_{petro} is the Petrosian radius. The mean surface brightness within the r_{petro} is used to define threshold of flux, then the pixel value above the threshold is assigned to the galaxy in the segmentation map. Both the Gini and M_{20} are calculated on the

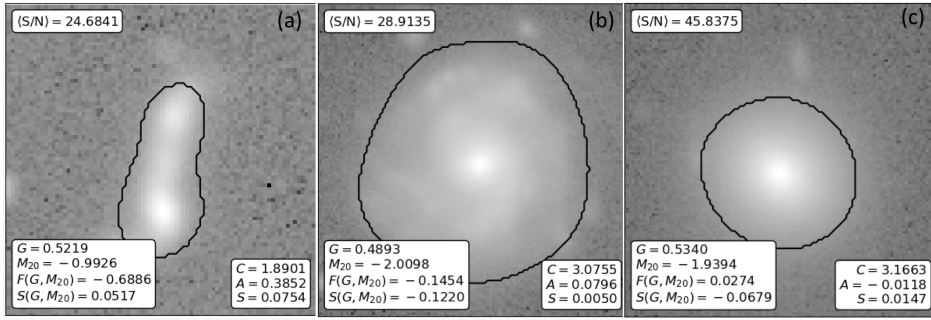


Figure 4. Example of the morphological measurements for the galaxy performed by *statmorph*. (a), (b), (c) are example images of mergers, Spiral, and Elliptical galaxies, respectively. Black solid contours represent segmentation maps and text labels represent the values of the Gini, M_{20} and CAS. $F(G, M_{20})$ and $S(G, M_{20})$ show that bulge statistic and merger statistic. Detailed parameter description is in [Rodríguez-Gomez et al. \(2019\)](#).

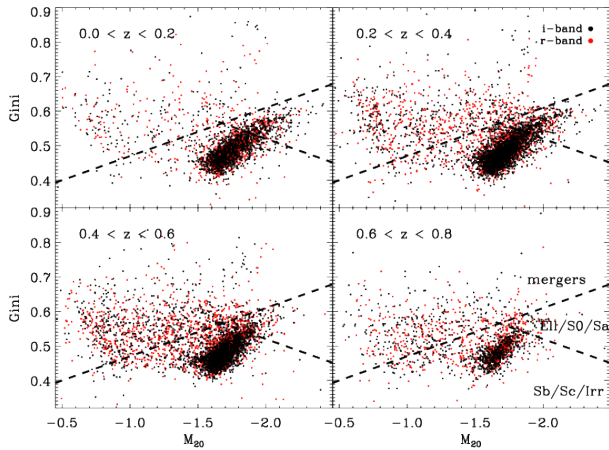


Figure 5. The Gini– M_{20} diagram for galaxies at different redshift ranges. Red and black dots represent galaxies in r and i band, respectively. Dashed lines separate the regimes according to their morphological types; mergers in above the dashed line, Ellipticals in right regime, and Spirals in below the dashed line.

segmentation map. Figure 4 shows the examples of segmentation maps of three galaxies with measured Gini and M_{20} . It should be noted that the high-column density of dust could impact the morphological classification of galaxies in the Gini– M_{20} space ([Lotz et al. 2008](#)). To briefly test this effect, we examine the distributions of Gini and M_{20} for Herschel detected and non-detected galaxies. Because the Herschel detection requires larger submm flux densities (i.e. larger amount of dust than those with similar $M_*/\text{SFRs}/T_{\text{dust}}$; [Hildebrand 1983](#), this comparison can show the impact of dust on the morphological measurements. The comparison does not show any systematic differences of Gini and M_{20} estimates between the two samples (not shown here), which is supported by the Kolmogorov-Smirnov test with high significance levels ($p < 0.35$). We therefore do not think that the dust introduces a systematic bias in our measurements of Gini and M_{20} parameter.

As [Lotz et al. \(2008\)](#) proposed criteria to separate galaxies into three galaxy types on the Gini - M_{20} diagram using galaxies at $0.2 < z < 1.2$, we adopt the classification criteria from the equation (4) of [Lotz et al. \(2008\)](#) to divide galaxies

into mergers, Spirals and Ellipticals on the Gini and M_{20} diagram: Mergers: $G > -0.14 M_{20} + 0.33$, E/S0/Sa: $G < -0.14 M_{20} + 0.33$, and $G > 0.14 M_{20} + 0.80$, Sb/Sc/Irr: $G \leq -0.14 M_{20} + 0.33$, and $G \leq 0.14 M_{20} + 0.80$.

Figure 5 shows the G– M_{20} distribution of our sample on r -, i -band images for different redshift bins. We find that the distribution of these two morphological parameters for galaxies on r -, i -band images are not significantly different. We derive morphological parameters for both r - and i -band images to select the one that gives similar rest-frame wavelengths for the comparison of galaxies at different redshifts. Therefore, we adopt the parameters from r -band images for the galaxies at $z < 0.2$, and from i -band images for those at $z > 0.2$. To verify our morphological classification based on the measurements of Gini and M_{20} , we also conduct the visual inspection of the optical images of all the galaxies in our sample. We find that only 1% of the galaxies classified as mergers in our sample turn out to be spirals, and 1.7% of ellipticals and 0.2 % of spirals based only on the G– M_{20} classification are mergers. This contamination is small enough to have no significant impact on our result. We therefore decided to keep the results based on the automated classification based on the estimates of Gini and M_{20} to avoid any possible subjective misclassification based on visual classification, especially for faint galaxies. Also, since the FWHM of a point source in the i -band images is 0.84 arcsec corresponding to ~ 3.8 kpc at our median redshift (i.e. $z \sim 0.3$), we could hardly find patchy features of star formation in the galaxy images that could affect the Gini during visual inspection of galaxies.

4 RESULTS

It has been well known that the infrared luminosity of galaxies is closely related to the merger activity of galaxies ([Hwang et al. 2007](#); [Ellison et al. 2013](#); [Larson et al. 2016](#)). However, the situation can differ if we consider a wide range of redshift. For example, Figure 6 shows the merger fraction of galaxies in our sample as a function of infrared luminosity at different redshift ranges. As expected, the merger fraction increases with L_{TIR} for a given redshift range. However, because the merger fraction could be different depending on the redshift despite similar L_{TIR} , we examine the merger fraction focusing on star formation mode.

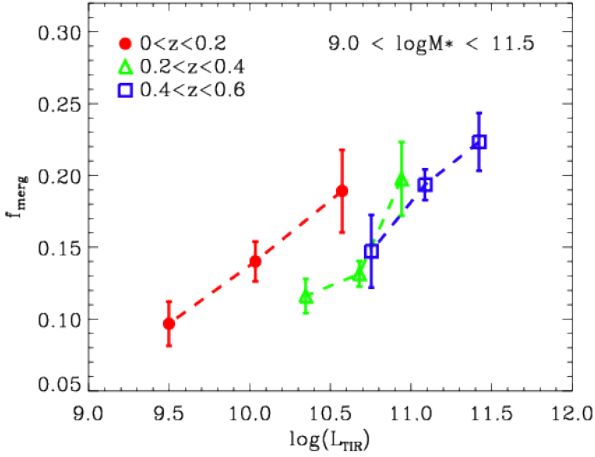


Figure 6. Merger fractions as a function of L_{TIR} at different redshift. Filled red circle, open green triangle, open blue rectangle represent galaxies at $0.0 < z < 0.2$, $0.2 < z < 0.4$, $0.4 < z < 0.6$, respectively.

4.1 Merger fractions of galaxies at different star formation modes

The relation between star formation rate and stellar mass of galaxies is tightly related to the star formation mode. To investigate the cosmic evolution out to $z \sim 1$ over the star formation mode, we divide our sample at each redshift bin (see Figure 7). We adopt the average SFR of main sequence galaxies with stellar mass and redshift from the equation (9) of Schreiber et al. (2015) to resolve star formation modes. They present an analysis of statistical properties of star-forming galaxies using the *Herschel* and *Hubble H*-band images in the redshift range of $z > 0.3$. We extrapolate their relation to $0 < z < 0.2$ bin, but found that the extrapolated SFRs are higher than those of previous studies (Brinchmann et al. 2004; Elbaz et al. 2007). Therefore, we used the relation derived from the galaxies at low redshifts (i.e. SDSS galaxies $z \approx 0.1$, Elbaz et al. 2007) to adjust the extrapolated relation; we set the average SFR of main sequence to be equal to that of SDSS at $\log(M_*/M_\odot) = 10.0$ in the redshift range with $0.0 < z < 0.2$, as shown in the left top panel of Figure 7. We define the galaxies within 2 and 0.5 times the average SFRs (dashed lines in Figure 7) as main sequence (MS) galaxies. Galaxies above the upper dashed line are considered as starbursts (SB, $SFR > 2 \times SFR_{MS}$), and galaxies below the lower dashed line as quiescent galaxies (QS, $SFR < 0.5 \times SFR_{MS}$). Our samples are distributed in three different star formation modes at $0.0 < z < 0.2$, however there are fewer quiescent galaxies as redshift increases because of the MIR detection limit. Note that quiescent galaxies becomes much fainter in the MIR ranges at higher redshift. Therefore, we constrain the galaxies mass range of $9.0 < \log(M_*/M_\odot) < 11.5$ as total sample to avoid extreme mass range of galaxies and select the uniform sample over the star formation mode.

To better understand the overall star formation activity for galaxies by minimising the mass effects, we plot the starburstiness (R_{SB}) distribution in Figure 8. Starburstiness represents the star formation activity which is a measure of the excess in specific star formation rate of a galaxy com-

pared to that of a main sequence galaxy with the same stellar mass and is defined as $R_{SB} = sSFR/sSFR_{MS}$ (Elbaz et al. 2011). Figure 8 displays R_{SB} of galaxies in total mass range $9.0 < \log(M_*/M_\odot) < 11.5$ (black solid histogram) and those at $10.5 < \log(M_*/M_\odot) < 11.5$ (blue dashed histogram). The galaxies with $R_{SB} < 0.5$ and $2 < R_{SB}$ represent quiescent and starburst systems, respectively. As expected, both samples show peaks around $R_{SB} = 1$. However, the bin of $0.6 < z < 0.8$ has fewer quiescent and main sequence galaxies than other bins because of detection limit. Therefore we remove the sample in $0.6 < z < 0.8$ for further analysis. Because the quiescent galaxies could be still affected by detection limits at all redshifts bins except $0.0 < z < 0.2$, it should be noted that the merger fractions of quiescent galaxies mean upper limits.

Figure 9 shows the evolution of merger fractions for starbursts, main sequence, and quiescent galaxies as a function of the redshift. We define the merger fraction as the ratio of a number of merging galaxies to total number of galaxies in each star formation mode within the redshift range. To minimise the mass effects on the comparisons of merger fractions between the samples, we examine the trend of galaxies with total ($9.0 < \log(M_*/M_\odot) < 11.5$) and narrow ($10.5 < \log(M_*/M_\odot) < 11.5$) mass range in the left and right, respectively. We find that merger fractions of all three different modes of galaxies marginally increase with redshift in both panels of different mass ranges. The merger fractions of galaxies in the total mass range at $0.0 < z < 0.2$ are higher compared to those of galaxies in the narrow mass range. This is because there are more galaxy samples in the $\log(M_*/M_\odot) < 10.5$ as shown in Fig 7. We also find that the merger fractions of galaxies differ for three star formation modes, and the merger fractions of starbursts are higher than those of main sequence and quiescent galaxies in both panels.

We fit the merger fractions evolution with power-law (Patton et al. 2002; Conselice, Yang & Bluck 2009), which is given by $f_m = \alpha(1+z)^m + C$. We use six points of merger fraction with binsize 0.1 of redshift. For starbursts and main sequence galaxies, we obtain the index $m = 0.90 \pm 0.18$ and 2.04 ± 0.13 in total mass range, respectively, and $m = 1.81 \pm 0.12$ and 1.21 ± 0.08 in narrow mass range, respectively. These are relatively similar or lower than those of others (Conselice et al. 2003; Lotz et al. 2008; Qu et al. 2017).

To examine whether our results are robust against different main sequence selections, we also use the evolutionary trend of main sequence locus in Pearson et al. (2018). Following the single power-law they used, $S = \alpha [\log(M_*) + 10.5] + \beta$ (Pearson et al. 2018; Whitaker et al. 2012), where α and β is the slope and the normalisation, respectively, we calculate the fit of SFR and M_* of galaxies. We fix the α as 0.5 and interpolate the β using the parameters from the table 2 in Pearson et al. (2018), and identify starbursts, main sequence and quiescent galaxies. We analyse merger fractions of galaxies and find that the increase trends of merger fractions for galaxies in different star formation modes as the redshift increase, when we use both the average SFRs of Schreiber et al. (2015) and Pearson et al. (2018), are consistent.

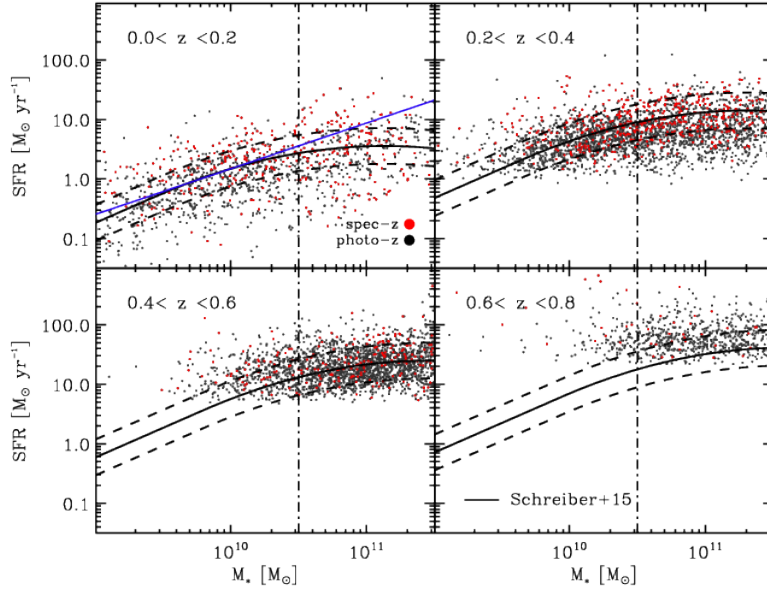


Figure 7. Star formation rates for 9- μm selected galaxies as a function of stellar mass at different redshift range. Solid line represents the average SFR for main sequence galaxies (Schreiber et al. 2015) and upper and lower dashed lines represent a factor of two above and below of this fit at each redshift range. Dash-dotted line represents $\log(M_*) = 10.5$. Blue solid line shows the best fits for the main sequence galaxies in SDSS (Elbaz et al. 2007). Red and black dots represent the galaxies with spec-z and photo-z, respectively.

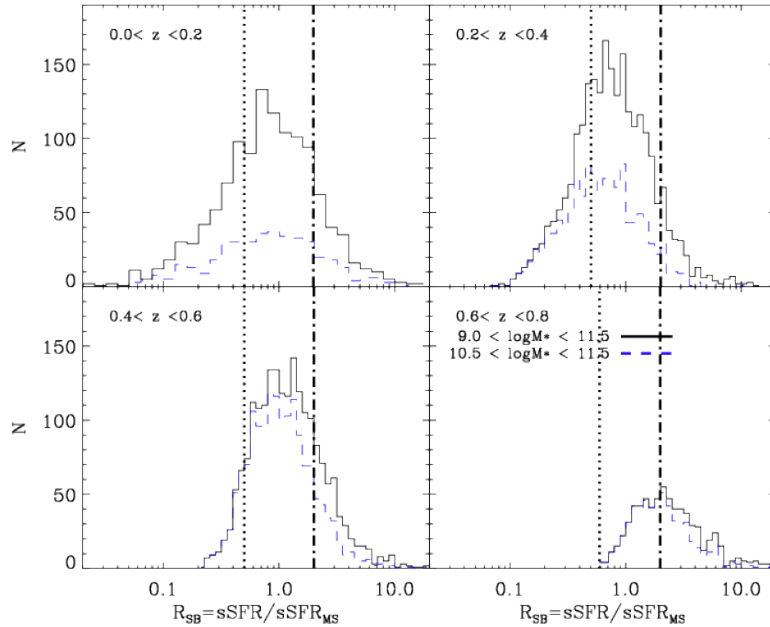


Figure 8. Starburstiness R_{SB} distribution of galaxies at each redshift range. Black solid and blue dashed line represent the galaxies in the stellar mass range of $9.0 < \log(M_*/M_\odot) < 11.5$ and $10.5 < \log(M_*/M_\odot) < 11.5$, respectively. Dotted and dash-dotted line represent the borders between starbursts and main sequence, main sequence and quiescent galaxies, respectively.

4.2 Merger fraction of galaxies with and without *Herschel* detections

It is well known that FIR bright galaxies tend to be found as mergers at low redshifts. However, this is not always true for high redshift galaxies; isolated disk galaxies at high redshifts can have high infrared luminosities without any

merger events because of their large amount of gas (Drew et al. 2020). This suggests that the infrared luminosity may not reflect genuine physical conditions of galaxies when comparing galaxies at different redshifts. Instead, it is important to distinguish galaxies based on more physically motivated parameters including star formation mode, which is the main driver of this study. To better justify this point, we fur-

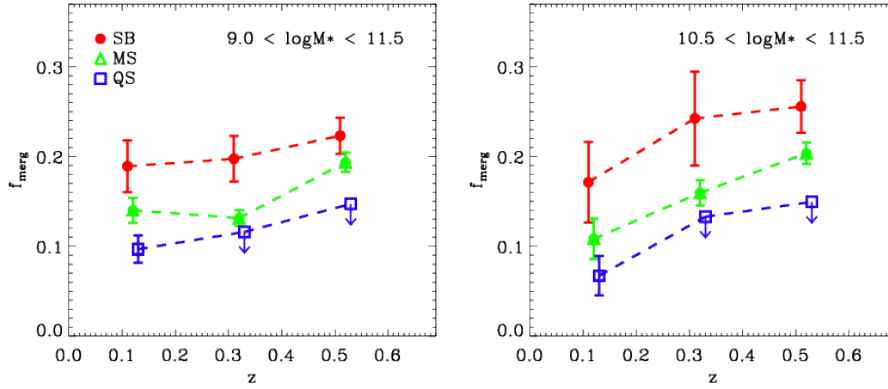


Figure 9. Evolution of the merger fractions for starburst, main sequence, and quiescent galaxies. Filled red circle, open green triangle, open blue rectangle represent starbursts, main sequence, and quiescent galaxies, respectively. Left panel shows galaxies in the entire stellar mass range, and right panel shows the galaxies in $10.5 < \log(M_*/M_\odot) < 11.5$.

then examine the merger fraction of FIR detected galaxies depending on the redshift and star formation modes with that of FIR non-detected galaxies. Here, the FIR detection means that the galaxies are detected at least one band of *Herschel*/SPIRE 250, 350 and 500 μm wavelengths. Because the *Herschel*/PACS covers only the NEP-Deep field unlike the *Herschel*/SPIRE (see Fig. 1 in Kim et al. 2021), we use the only the *Herschel*/SPIRE data to reduce the selection effect for the comparison.

We separate our 9 μm detected samples into *Herschel* non-detected and detected ones, and show their starburstiness at different redshift bins in Figure 10. Black dashed and blue solid lines represent *Herschel* detected and non-*Herschel* detected sample, respectively. We find that *Herschel* detected samples have higher R_{SB} than those of non-*Herschel* detected sample in all redshift bins as we can expect. Figure 11 shows the evolution of galaxy merger fraction for non-*Herschel* detected and *Herschel* detected samples in upper and bottom panels, respectively. Right and left panels show the total and narrow mass range, respectively. In the total mass range, we find that the merger fraction of starburst galaxies with *Herschel* detections seemingly increase as the redshift increases compared to those of non-*Herschel* detected galaxies. Also, the merger fraction of those with *Herschel* detections is higher than those of non-*Herschel* detected galaxies, because of *Herschel* detected galaxies have higher FIR luminosities.

We fit the merger fractions evolution with power-law (Patton et al. 2002; Conselice, Yang & Bluck 2009), which is given by $f_m = \alpha(1+z)^m + C$. For non-*Herschel* detected galaxies, we obtain the index $m = 0.18 \pm 0.62$ and 0.81 ± 0.19 in total mass range and $m = 0.46 \pm 2.29$ and 1.44 ± 2.12 in narrow mass range for starbursts and main sequence galaxies, respectively. For *Herschel* detected galaxies, we obtain the index $m = 2.22 \pm 0.72$ and 1.09 ± 0.78 in total mass range and $m = 2.71 \pm 2.46$ and 1.78 ± 2.04 in narrow mass range for starbursts and main sequence galaxies, respectively. The indices for merger fractions of starbursts in *Herschel* detected galaxies are significantly different compared to those in non-*Herschel* detected galaxies. The comparison of them are such as $m = 0.18 \pm 0.62$ vs. $m = 2.22 \pm 0.72$ in total mass range, and $m = 0.46 \pm 2.29$ vs. $m = 2.71 \pm 2.46$ in narrow mass range. The differences of main

sequence galaxies are relatively weak compared to those of starbursts such as $m = 0.81 \pm 0.19$ vs. $m = 1.09 \pm 0.78$ in total mass range, and $m = 1.44 \pm 2.12$ vs. $m = 1.78 \pm 2.04$ in narrow mass range.

We also examine that the *Herschel* detected samples have large range of SFRs at low redshift, and the SFRs of those galaxies become higher as the redshift increases. Thus, the increase tendency of merger fractions for *Herschel* detected samples may includes the cosmic evolution. To better compare the merger fractions between *Herschel* detected and non-*Herschel* detected galaxies by minimising the mass effects, we compare the results in narrow mass range in the right panels of Figure 11. Although errors are large, we find that the fraction at the same star formation mode is not different depending on the *Herschel* detection considering the errors. Of course, the merger fractions of different star formation modes are still different for both samples. This comparison shows the importance of star formation mode in determining the merger fraction regardless of FIR luminosities.

5 DISCUSSION

5.1 Merger fractions over the star formation modes and their evolution

The evolution of galaxy merger fraction over the cosmic time has been examined through numerical simulations and observational analysis. Some simulations assuming cold dark matter Universe predicted a decreasing merger fraction of galaxies with cosmic time (Fakhouri & Ma 2008; Rodriguez-Gomez et al. 2015), while other simulations show that the increasing of merger fraction to $z \sim 1.5$ and then constant as redshift increases (Kaviraj et al. 2015; Qu et al. 2017; Snyder et al. 2017). In observations, Conselice et al. (2008) showed that the merger fraction of very massive galaxies with $\log(M_*/M_\odot) > 10$ appears to increase up to $z \sim 3$, while the merger fraction of less massive galaxies has a peak $z \sim 1.5 - 2.5$ and decreases to high redshift. Ventou et al. (2017) also showed that the merger fractions for galaxies with $\log(M_*/M_\odot) > 9.5$ increase to around $z \sim 2$ and slowly decrease after that. Even in relatively low redshift range,

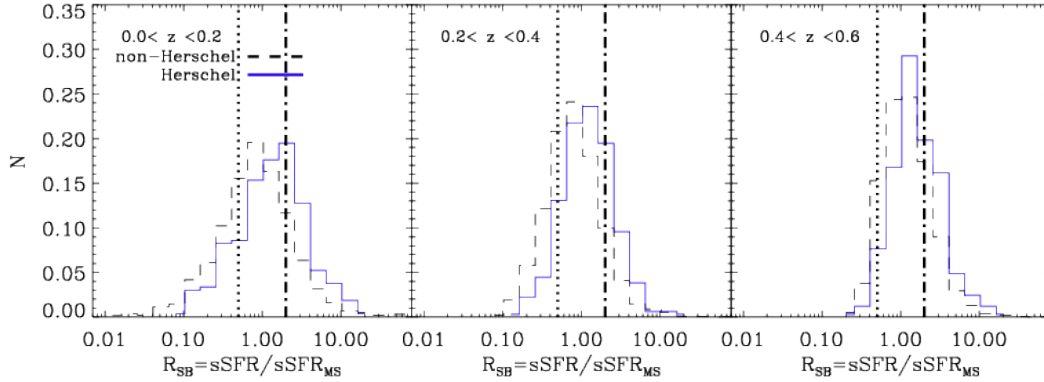


Figure 10. Distribution of starburstiness for galaxies at each redshift range. Black dashed line represents non-*Herschel* detected galaxies and blue solid line represents *Herschel* detected galaxies.

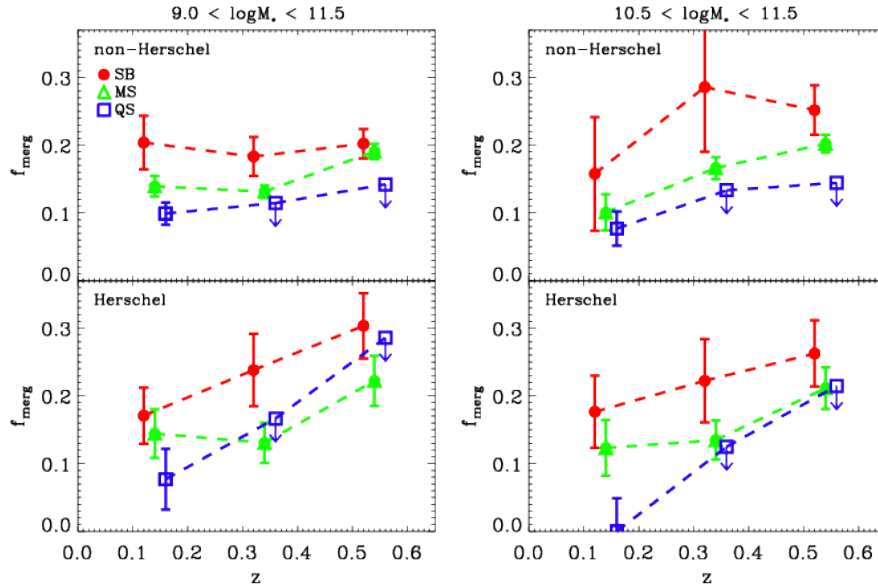


Figure 11. Evolution of the merger fraction of starburst, main sequence, and quiescent galaxies for non-*Herschel* detected galaxies (upper) and *Herschel* detected galaxies (bottom). The left and right panels show galaxies with total and fixed mass range of $9.0 < \log(M_*/M_\odot) < 11.5$ and $10.5 < \log(M_*/M_\odot) < 11.5$. Coloured symbols are same as Fig 9.

some authors found an increasing merger fraction with redshift (López-Sanjuan et al. 2009; Ventou et al. 2017), however constant merger fraction at $z < 0.6$ is also suggested (Conselice, Yang & Bluck 2009; Jogee et al. 2009). Our results are in agreement with the observations suggesting that the merger fraction of galaxies slightly increases with redshift $z < 0.6$ (López-Sanjuan et al. 2009; Man, Zirm & Toft 2016; Ventou et al. 2017). However, the absolute values of merger fractions could differ due to different methods of sample selections depending on luminosity, mass or definition of a merger, which will be discussed in Section 5.3.

As shown Figure 9, merger fractions of starburst, main sequence and quiescent galaxies are dependent of star formation mode. Although some authors suggested the dependency of merger fraction of galaxies on the distance from the main sequence (Cibinel et al. 2019; Pearson et al. 2019), the effect of star formation modes could not be evaluated quantitatively. For the fair comparison, we try to investigate the

evolution of merger fraction for galaxies with similar star formation activities.

Merger galaxies selected by morphology are mainly late-stage and disturbed systems (Pearson et al. 2019). Because our merger galaxy samples are also selected by morphology, the higher merger fraction in this study than those in other studies can suggest that the star formation enhancement is prominent at the late stage of merging (Sanders & Mirabel 1996; Haan et al. 2011; Cox et al. 2006; Hwang et al. 2012) and earlier stage of merging only cause mild increase of SFRs for close pairs (Lin et al. 2007).

Regarding the evolution of merger fraction, Conselice, Yang & Bluck (2009) showed diverse results through the fitting with a power-law function. They found that the power-law slope changes from 1.5 to 3.8 depending on sample selection and different merger fraction at $z = 0$. The slope tend to be higher for more massive galaxies and lower for less massive galaxies (Conselice et al. 2003). Qu et al. (2017)

used an exponential power-law function for the simulation predictions, they found that the power-law slope, m , for close pairs with $z < 4$ changes from 2.8 to 3.7 depending on the mass limits. Otherwise, others who used morphological disturbances for merger selections and the redshift range of galaxies with $z < 1.2$ (Lotz et al. 2008) obtained the mild slope of $m = 1.26$. Considering similar merger selection and redshift range, our results on the power-law slope of $m = 0.18 - 2.71$ are consistent with those from Lotz et al. (2008). However, they showed that the slope of merger fraction could be easily affected by morphological diagnostics and timescales to determine merger fractions.

5.2 Mergers for *Herschel* detected galaxies

Galaxy merging is expected to drive star formation episodes (Barnes & Hernquist 1996; Mihos & Hernquist 1996), however, UV/optical light is dimmed and sources appear redder due to absorption and scattering by dust. Since considerable amounts of the energy from star formations and AGNs have been absorbed by gas and dust and re-emitted in FIR wavelengths (Puget et al. 1996; Dole et al. 2006), FIR data set would be good for the study of star formation activity (Pei, Fall & Hauser 1999; Chary & Elbaz 2001). Some results for LIRGs and ULIRGs showed that FIR-bright galaxies are ongoing mergers and have disturbed morphology, which are the evidence for merger activities (Sanders et al. 1988; Clements et al. 1996; Hopkins et al. 2006; Hwang et al. 2010). While these studies were mainly focused on FIR-bright galaxies, our samples selected from MIR detections have a wider range of L_{TIR} . As shown in Figure 9 and 11, the merger fractions are strongly dependent of star formation modes, irrespective of *Herschel* detection. We also find that the increasing slope of merger fraction for starbursts detected in *Herschel* is steeper than that of non-*Herschel* detected starbursts. The difference of the slope for main sequence galaxies is not significant compared to those of starbursts. Note that quiescent galaxies shows the steepest slope, however merger fractions at $z > 0.2$ are upper limit due to the lack of sample. These results could support that *Herschel* detected galaxies with high FIR luminosity such as LIRGs/UIRGs are more stochastically in the merging stage. Although it is difficult to compare with other results in the effectiveness of FIR detection, this can be interpreted that the merger fractions of galaxies are determined not only by the IR luminosity, but also by the star formation mode of galaxies at fixed redshift range.

5.3 Comparison to other studies

To study the merger fraction of galaxies, one has to define a galaxy sample along with redshift/mass range and galaxy classification method (Lotz et al. 2008; Conelice, Yang & Bluck 2009; Bundy et al. 2009; Man, Zirm & Toft 2016; Delahaye et al. 2017; Watson et al. 2019). Therefore, it is important to understand the sample selection including the merger identification scheme to make fair comparison with other studies. Although it is difficult to directly compare our results with other studies because of these differences, we describe the similarity and the difference between our study and other studies in this section.

Methodologically, merger galaxies can be identified by using galaxy pairs or morphological disturbances. As morphological cases, Lotz et al. (2008) used Gini and M_{20} for selecting merger galaxies in $0.2 < z < 1.2$ and volume limited sample with B-band luminosity limits assuming the luminosity evolution. They found weak evolution of the merger fractions of galaxies in this redshift range. Conelice, Yang & Bluck (2009) derived the increasing merger fraction using asymmetry and clumpiness with galaxies from COSMOS and EGS between $0.2 < z < 1.2$. Although there are differences between our sample and theirs such as redshift range and existence of MIR data, our result is consistent with the previous ones (Lotz et al. 2008; Conelice, Yang & Bluck 2009) that the merger fractions for galaxies mildly increase as redshift increases with using morphological selection for merger galaxies.

In addition to morphological method, there are studies of merger fractions using galaxy pairs. Bundy et al. (2009) and de Ravel et al. (2009) use mass-selected pairs and projected separation (R_{proj}) for selecting merger galaxies, respectively. Watson et al. (2019) showed that the merger fraction for paired galaxies in clusters is higher than those in field environments (Bundy et al. 2009; de Ravel et al. 2009). Cibinel et al. (2019) compared the results from the morphological classification with those from the pair identification. They found that most of the starbursts galaxies are morphologically disturbed, but for galaxy pairs, the merger fractions were small in starburst galaxies. Thus, this can suggest that the merger fractions of this study could be higher than that in other studies based on galaxy pairs.

Relatively high merger fractions of our results also can be explained by sample selection criteria. Lotz et al. (2008) used luminosity-size limits for selecting of massive galaxies. Conelice, Yang & Bluck (2009); López-Sanjuan et al. (2009) used galaxies with $M_* > 10^{10} M_{\odot}$. These criteria secure limited galaxies compared to our sample that have mass range of $9.0 < \log(M_*/M_{\odot}) < 11.5$. However, the largest difference of the sample selection between ours and others is the use of the MIR detection in our study, which can significantly affect the star formation activity. Then, the number of sample can be limited, this small total number of sample which is denominators of merger fractions could affect that the merger fractions of galaxies become high compared to others. The method also can affect results; because Gini- M_{20} are sensitive to the features of minor mergers (Lotz et al. 2011), our method may select more merger candidates than other studies based on CAS or asymmetry criteria. Pearson et al. (2019) reported elevated merger fraction for galaxies at $0 < z < 4$ based on CANDELS data compared to other studies. Such a result may be arisen because the pixel size of galaxies within the images becomes smaller and galaxies become fainter as redshift increases, then the suppressed galaxy features counted as merger galaxies. Therefore, the direct comparison of absolute values of merger fractions between different studies is difficult.

6 SUMMARY

We used the galaxy sample detected at the MIR band ($9 \mu\text{m}$) of AKARI in the NEP-Wide field. In order to identify the merging galaxies, the morphological analyses were carried

out relying on the Gini and M_{20} coefficients derived from deep Subaru/HSC (r -, i -band) images. Using the spectroscopic and photometric redshifts, we derived total infrared luminosity and SFR from AKARI 9 μm detections. We compare the merger fractions between three different star formation modes at $z < 0.6$: starburst, main sequence and quiescent galaxies. Our main results are as follows:

(i) The merger fractions for starbursts, main sequence, and quiescent galaxies slightly increase with redshift at $z < 0.6$.

(ii) The galaxy merger fractions differ depending on the star formation mode. The starbursts show higher merger fractions than those of main sequence and quiescent galaxies.

(iii) The increasing slope of the merger fractions for *Herschel* detected starbursts slightly steeper compared to those of non-*Herschel* detected starbursts.

Our results are in line with the idea that the merger fraction increases with redshift in local Universe (Lotz et al. 2008; Conselice, Yang & Bluck 2009; López-Sanjuan et al. 2009) and galaxies in the different star formation modes such as starbursts, main sequence and quiescent galaxies show different merger fractions (Cibinel et al. 2019; Pearson et al. 2019). Regardless of the FIR detection, the increasing trends of the merger fraction over local universe ensure the consistency in all the different star formation modes. These results underscore the importance of the star formation mode in the study of evolution of galaxy merger fraction. To better understand the merger fraction evolution with different star formation activities, it is important to secure a larger, unbiased sample of high- z galaxies, which does not suffer from observational selection effects on the star formation mode.

ACKNOWLEDGEMENTS

W-SJ, EK and Y-SJ acknowledges support from the National Research Foundation of Korea (NRF) grant funded by the Ministry of Science and ICT (MSIT) of Korea (NRF-2018M1A3A3A02065645). HSH was supported by the New Faculty Startup Fund from Seoul National University. HShim acknowledges the support from the National Research Foundation of Korea grant No. 2018R1C1B6008498. TH is supported by the Centre for Informatics and Computation in Astronomy (CICA) at National Tsing Hua University (NTHU) through a grant from the Ministry of Education of the Republic of China (Taiwan).

DATA AVAILABILITY

The data underlying this article will be shared on reasonable request to the corresponding author.

REFERENCES

Abraham R. G., van den Bergh, S., & Nair P., 2003, ApJ, 588, 218
 Arnouts S. et al., 1999, MNRAS, 310, 540
 Barnes J. E., Hernquist L., 1996, ApJ, 471, 115
 Barnes J. E., 2004, MNRAS, 350, 798

Bundy K., Fukugita M., Ellis R. S., Targett T. A., Belli S., Kodama T., 2009, ApJ, 697, 1369
 Bohlin, R. C. et al., 1991, ApJ, 368, 12
 Brinchmann J., Charlot S., White S. D. M., Tremonti C., Kauffmann G., Heckman T., Brinkmann J., 2004, MNRAS, 351, 1151
 Burgarella D., Buat V., Iglesias-Páramo J., 2005, MNRAS, 360, 1413
 Calzetti D., Wu S.-Y., Hong S., Kennicutt R. C., Lee J. C., Dale D. A., Engelbracht C. W., et al., 2010, ApJ, 714, 1256
 Clements D. L., Sutherland W. J., McMahon R. G., Saunders W., 1996, MNRAS, 279, 477
 Chabrier G., 2003, PASP, 115, 763
 Chary R., Elbaz D., 2001, ApJ, 556, 562
 Cibinel A. et al., 2019, MNRAS, 485, 5631
 Conselice C. J., Bershady M. A., Jangren A., 2000, ApJ, 529, 886
 Conselice C. J., et al., 2003, AJ, 126, 1183
 Conselice C. J., 2006, MNRAS, 373, 1389
 Conselice C. J., Rajgor S., Myers R., 2008, MNRAS, 386, 909
 Conselice C. J., Yang C., Bluck A. F. L., 2009, MNRAS, 394, 1956
 Covington M., Dekel A., Cox T. J., Jonsson P., Primack J. R., 2008, MNRAS, 384, 94
 Cox T. J., Jonsson P., Primack J. R., Somerville R. S., 2006, MNRAS, 373, 1013
 Cox T. J., Jonsson P., Somerville R. S., Primack J. R., Dekel A., 2008, MNRAS, 384, 386
 Daddi E. et al., 2007, ApJ, 670, 156
 De Lucia G., et al., 2006, MNRAS, 366, 499
 Delahaye A. G. et al., 2017, ApJ, 843, 126
 de Ravel L. et al., 2009, A&A, 498, 379
 Drew P. M., Casey C. M., Cooray A., Whitaker K. E., 2020, ApJ, 892, 104
 Dole H. et al., 2006, A&A, 451, 417
 Draine B. T., Li A., Hensley B. S., Hunt L. K., Sandstrom K., Smith J.-D. T., 2020, arXiv, arXiv:2011.07046
 Duncan K. et al., 2019, ApJ, 876, 110
 Elbaz D., Cecarsky C. J., 2003, Science, 300, 270
 Elbaz D. et al., 2007, A&A, 575, A74
 Elbaz D. et al., 2011, A&A, 533, A119
 Ellison S. L. et al., 2013, MNRAS, 430, 3128
 Fakhouri O., Ma C.-P., 2008, MNRAS, 386, 577
 Galametz M., Kennicutt R. C., Calzetti D., Aniano G., Draine B. T., Boquien M., Brandl B., et al., 2013, MNRAS, 431, 1956
 Glasser G. J., 1962, American Stat. Assoc. 57, 648, 654
 Goto T. et al., 2017, PKAS, 32, 225
 Goto T. et al., 2018, The Cosmic Wheel and the Legacy of the AKARI Archive: From Galaxies and Stars to Planets and Life, 189
 Haan S. et al., 2011, AJ, 141, 100
 Hao C.-N., et al., 2011, ApJ, 741, 124
 Hildebrand R. H., 1983, QJRAS, 24, 267
 Ho S. C.-C., Goto T., Oi N., Kim S. J., Malkan M. A., Pollo A., Hashimoto T., et al., 2021, MNRAS, 502, 140
 Huang T.-C. et al., 2020, arxiv:2008.05224
 Hwang N. et al., 2007, ApJS, 172, 583
 Hwang H. S., Serjeant S., Lee M. G., et al., 2007, MNRAS, 375, 115
 Hwang H. S., Park, C., 2009, ApJ, 700, 791
 Hwang H. S., Elbaz D., Lee J. C., Jeong W.-S., Park C., Lee M. G., Lee H. M., 2010, A&A, 522, A33
 Hwang H. S., Geller M. J., Kurtz M. J., et al. 2012, ApJ, 758, 25
 Hopkins P. F., Somerville R. S., Hernquist L., Cox T. J., Robertson B., Li Y., 2006, ApJ, 652, 864
 Ilbert O. et al., 2006, A&A, 457, 841
 Jarrett T. H. et al., 2011, ApJ, 735, 112
 Jeon Y. et al., 2010, ApJS, 190, 166
 Jeon Y. et al., 2014, ApJS, 214, 20

- Jogee S. et al., 2009, ApJ, 697, 1971
- Kado-Fong E., Greene J. E., Hendel D., Price-Whelan A. M., Greco J. P., Goulding A. D., Huang S., et al., 2018, ApJ, 866, 103
- Kampczyk P., Lilly S. J., Carollo C. M. et al. 2007, ApJS, 172, 329
- Kartalpe J. S. et al., 2010, ApJ, 721, 98
- Kaviraj, S., Devriendt, J., Dubois, Y., et al. 2015, MNRAS, 452, 2845
- Kennicutt R. C., Evans N. J., 2012, ARA&A, 50, 531
- Kim J.-h., Wise J. H., Abel T., 2009, ApJ, 694, L123
- Kim S. J. et al., 2012, A&A, 548, A29
- Kim, H. K. et al., 2018, JAXA-SP-17-009E, 371-374
- Kim S. J., Oi N., Goto T., Ikeda H., Ho S. C.-C., Shim H., Toba Y., et al., 2021, MNRAS, 500, 4078
- Kuchinski L. E., Freedma, W. L., Madore B. F. et al. 2000, ApJS, 131, 441
- Larson K. L. et al., 2016, ApJ, 825, 128
- Lin L. et al., 2007, ApJL, 660, L51
- López-Sanjuan C., Balcells M., Pérez-González P. G., Barro G., García-Dabó C. E., Gallego J., Zamorano J., 2009, A&A, 501, 505
- Lotz J. M., Primack J., Madau P., 2004, AJ, 128, 163
- Lotz J. M. et al., 2008, ApJ, 672, 177
- Lotz J. M. et al., 2010, MNRAS, 404, 590
- Lotz J. M. et al., 2010, MNRAS, 404, 575
- Lotz J. M. et al., 2011, ApJ, 742, 103
- Nayyeri H. et al., 2018, ApJS, 234, 38
- Noll S. et al. 2009, A&A, 507, 1793
- Man A. W. S., Zirm A. W., Toft S., 2016, ApJ, 830, 89
- Mateos S. et al, 2012, MNRAS, 426, 3271
- Mantha K. B. et al., 2018, MNRAS, 475, 1549
- Menanteau F., Ford H. C., Motta V. et al., 2006, AJ, 131, 208
- Mihos, J. C., Hernquist, L. 1996, ApJ, 464, 641
- Murphy E. J. et al., 2011, ApJ, 737, 67
- Salpeter E. E., 1955, ApJ, 121, 161
- Shim H. et al., 2013, ApJS, 207, 37
- Ohyama Y. et al., 2018, A&A, 618, A101
- Oi N. et al., 2014, A&A, 566, A60
- Oi N. et al., 2017, PASJ, 69, 70
- Oi N., Goto T., Matsuhara H., Utsumi Y., Momose R., Toba Y., Malkan M., et al., 2021, MNRAS, 500, 5024
- Patton D. R. et al., 2002, ApJ, 565, 208
- Pearson C. et al., 2017, PKAS, 32, 219
- Pearson W. J. et al., 2018, A&A, 615, A146
- Pearson C. et al., 2019, PASJ, 71, 13
- Pei Y. C., Fall S. M., Hauser M. G., 1999, ApJ, 522, 604
- Puget J.-L., Abergel A., Bernard J.-P., Boulanger F., Burton W. B., Desert F.-X., Hartmann D., 1996, A&A, 308, L5
- Qu, Y., Helly, J. C., Bower, R. G. et al. 2017, MNRAS, 464, 1659
- Rodighiero G., Daddi E., Baronchelli I., et al., 2011, ApJ, 739, L40
- Rodriguez-Gomez V., Genel S., Vogelsberger M., et al., 2015, MNRAS, 449, 49
- Rodriguez-Gomez V., et al., 2019, MNRAS, 483, 4140
- Saitoh T. R. et al., 2009, PASJ, 61, 481
- Sanders D. B., et al., 1988, ApJ, 325, 74
- Sanders D. B., Mirabel I. F., 1996, ARA&A, 34, 749
- Schreiber C., et al., 2015, A&A, 575, A74
- Sérsic, J. L., 1963, BAAA, 6, 41
- Shogaki A. et al., 2018, JAXA-SP-17-009E, 367-370
- Snyder, G. F., Lotz, J. M., Rodriguez-Gomez, V., et al. 2017, MNRAS, 468, 207
- Smircina A., Smith J. D. T., Dale D. A., French K. D., Croxall K. V., Zhukovska S., Togi A., et al., 2018, ApJ, 855, 51
- Spinoglio L., Malkan M. A., Rush B., Carrasco L., Recillas-Cruz E., 1995, ApJ, 453, 616
- Springel V., Di Matteo T., Hernquist L., 2005, MNRAS, 361, 776
- Toomre A., Toomre J., 1972, ApJ, 178, 623
- Ventou E. et al., 2017, A&A, 608, A9
- Wang, T.-W., 2020, arXiv:2010.08225
- Watson C. et al., 2019, ApJ, 874, 63
- Whitaker, K. E., van Dokkum, P. G., Brammer, G., & Franx, M. 2012, ApJ, 754, L29
- Windhorst, R. A., Taylor, V. A., Jansen, R. A., et al. 2002, ApJS, 143, 113